

# Multichannel quantum defect theory and high-resolution spectroscopy of the hyperfine structure of high Rydberg states of $^{83}\text{Kr}$

H. J. Wörner, U. Hollenstein, and F. Merkt\*

*Laboratorium für Physikalische Chemie, ETH Zürich, CH-8093 Zurich, Switzerland*

(Received 15 May 2003; published 26 September 2003)

The hyperfine structure of  $ns$  and  $nd$  Rydberg states of  $^{83}\text{Kr}$  has been measured in the range  $n=30-190$  below the  $^2P_{3/2}$  ionization threshold by pulsed-field ionization following single-photon excitation from the  $^1S_0$  ground state using a narrow-bandwidth vacuum-ultraviolet laser system. A multichannel quantum defect theory (MQDT) treatment of the hyperfine structure in Rydberg states of the rare-gas atoms has been developed that quantitatively accounts for the effects of the nuclear spin on the spectral structures over the entire range of principal quantum number investigated. The model allows the parametrization of the hyperfine structure of the Rydberg states in terms of the ionic hyperfine structure and relies on the assumption that the interaction with the nuclear spin is negligible in the close-coupling region of the electron-ion collision, an assumption that is also expected to be valid in other atomic and molecular systems. Improved eigen quantum defects for the  $ns$  and  $nd$  Rydberg series with  $J=1$  and  $2$  have been derived from the MQDT analysis, and the hyperfine structure of the two  $^2P_{3/2}$  and  $^2P_{1/2}$  spin-orbit components of the ground state of  $^{83}\text{Kr}^+$  has been determined.

DOI: 10.1103/PhysRevA.68.032510

PACS number(s): 32.10.Fn, 32.80.Rm, 32.30.Jc, 34.60.+z

## I. INTRODUCTION

Multichannel quantum defect theory (MQDT) provides a compact and elegant treatment of electron-ion collisions that has greatly contributed to the current understanding of the photoabsorption and photoionization spectra of atoms and molecules below, between, and above the different ionization limits [1–4]. The theory successfully describes atomic and molecular photoabsorption and photoionization spectra in terms of the close-coupling properties of the electron-ion collision by means of frame transformations between the close-coupling and the long-range regions. In molecules, the transformation enables a smooth transition between Hund's case (a) or (b) at short range and Hund's case (d) or (e) at long range [4,5]. In rare-gas atoms, the frame transformation connects the close-coupling region which is well approximated by  $LS$  coupling to the asymptotic region which is adequately described by  $jj$  coupling [6].

The hyperfine structure of atomic and molecular Rydberg states and its treatment by MQDT have so far received little attention [7–9], primarily because of the lack of sufficiently resolved experimental data. Progress in experimental techniques in the past decade has been such that information on the hyperfine structure of high Rydberg states can now be derived by high-resolution laser spectroscopy [8–13] or by millimeter-wave spectroscopy [14,15]. A high-resolution (submegahertz) measurement of the hyperfine structure of  $ns$ ,  $np$ ,  $nd$ , and  $nf$  Rydberg states of ortho- $\text{H}_2$  in the range  $n=50-65$  by millimeter-wave spectroscopy [16,17] has recently stimulated a detailed analysis by MQDT [18]. This analysis, which could account for the finest details of the energy level structure, also yielded, by extrapolation, the hyperfine structure of the ground rovibronic state of ortho- $\text{H}_2^+$  and additional information on the  $p$  and  $f$  Rydberg states of

molecular hydrogen [18]. The success of this analysis and the desire to extend it to other systems represented the primary motivations of the present study of the hyperfine structure in high Rydberg states of  $^{83}\text{Kr}$  by high-resolution vacuum-ultraviolet laser spectroscopy and MQDT.

Other important reasons for choosing  $^{83}\text{Kr}$  for a combined experimental and theoretical study of the hyperfine structure in Rydberg states were, first, the availability of a large body of high-quality spectroscopic data on the Rydberg states of krypton [19–33], second, the fact that a very detailed MQDT analysis of the Rydberg spectra of the  $I=0$  isotopes has been carried out [34], and, finally, experimental convenience: The Rydberg states of krypton are easily accessible from the ground neutral state using narrow-bandwidth vacuum-ultraviolet (VUV) lasers, and mass-analyzed spectra of  $^{83}\text{Kr}$  (natural abundance 11.5%) can readily be obtained from natural probes of Kr following VUV laser excitation and pulsed-field ionization in a time-of-flight mass spectrometer.

Extensive tables of term values for the Rydberg states of krypton have been available for a long time [19,20], the latest and most extensive compilation being that of Sugar and Musgrove [21]. The  $s$  and  $d$  Rydberg states of the  $I=0$  isotopes [ $^{78}\text{Kr}$  (natural abundance 0.35%),  $^{80}\text{Kr}$  (2.25%),  $^{82}\text{Kr}$  (11.6%),  $^{84}\text{Kr}$  (57.0%),  $^{86}\text{Kr}$  (17.3%)] converging to the lower ( $^2P_{3/2}$ ) and upper ( $^2P_{1/2}$ ) spin-orbit components of the ground  $^2P$  term of  $\text{Kr}^+$  have been extensively studied by VUV photoabsorption and photoionization spectroscopy [22–25], by nonresonant and resonant two-photon excitation from metastable levels [26–31], and by electron energy loss spectroscopy [32]. Laser spectroscopic measurements of the  $p$  and  $f$  Rydberg states have also been reported [33], and the behavior of the Rydberg Stark states of Kr has been exploited to demonstrate that the translational motion of Rydberg atoms and molecules can be controlled by inhomogeneous electric fields [35].

The Rydberg spectra of the rare-gas atoms have played an important role in the development of MQDT and its early

\*Author to whom correspondence should be addressed.

application to the analysis of photoabsorption and photoionization spectra [6,36]. Detailed MQDT analyses of the  $ns$  and  $nd$  Rydberg series of krypton, particularly for  $J=1$  [32,37], but also for  $J=0, 2$ , and  $3$ , have been reported [31,34]. The most extensive MQDT study to date is that of Aymar *et al.* [34], who reported complete sets of MQDT parameters for the  $\ell=0$  and  $\ell=2$  ( $J=0-3$ ) channels, including eigenchannel quantum defects  $\mu_\alpha$ , their energy dependence, and the elements of the orthogonal transformation matrix  $U_{i\alpha}$  connecting the close-coupling eigenchannels  $\alpha$  to the fragmentation channels  $i$ . MQDT has also been applied in studies of the Stark effect in the Rydberg states of the rare-gas atoms [38].

A recurring theme in the study of the Rydberg states of the rare-gas atoms by MQDT is the deviation of the eigenchannels from purely  $LS$ -coupled channels, which is, among other factors, at the origin of the interaction and the mixing between the  $s$  and  $d$  series [31,32,34,36,37,39-41]. The  $s$ - $d$  interaction is particularly elusive in krypton because the separation between the  $^2P_{3/2}$  and  $^2P_{1/2}$  ionization thresholds is so large that the  $ns'$  and  $nd'$  levels are extremely sparse in the region below the  $^2P_{3/2}$  threshold where the  $ns$  and  $nd$  series are well developed. (Rydberg series labeled by a prime are commonly used to designate series converging on the upper spin-orbit component of the ion. The usual label for Rydberg states of the rare-gas atoms is thus  $n\ell[k]_J$  or  $n\ell'[k]_J$ , where  $k$  represents the quantum number of the angular momentum vector  $\vec{k}$  that results from the addition of  $\vec{\ell}$  to the total angular momentum of the ion core  $\vec{J}^+$ .) Consequently, it has proven difficult to distinguish the effects of the energy dependence of the eigen quantum defects on the energy level structure from the effects of the channel interactions induced by a departure from  $LS$  coupling.

Several high-resolution spectroscopic measurements have already been reported that provide information on the hyperfine structure of low- $n$  Rydberg states of  $^{83}\text{Kr}$ , the earliest measurements leading to the determination of the nuclear spin quantum number  $I=9/2$  [42,43]. Later studies [44-48] primarily focused on the hyperfine structure of the microwave, infrared, and visible spectra of metastable krypton Rydberg states and aimed at determining the term-dependent hyperfine constants. Trickl *et al.* [11] reported ultrahigh-resolution ( $1+1'$ ) resonance-enhanced two-photon ionization spectra of transitions from the  $^1S_0$  ground state to the  $5s[3/2]_1$ ,  $5s'[1/2]_1$ ,  $6s[3/2]_1$ ,  $6s'[1/2]_1$ , and  $7s[3/2]_1$  Rydberg states using a narrow-bandwidth VUV laser system and analyzed the hyperfine coupling parameters in terms of both  $LS$  and  $jj$  coupling. Brandi *et al.* [13] measured the hyperfine structure and determined the hyperfine coupling constants of the  $5p[5/2]_2$  Rydberg state. To our knowledge, no MQDT analysis of the hyperfine structure in any of the rare-gas atoms has been reported yet.

In the close-coupling region of the electron-ion collision, both the kinetic energy of the electron and its interaction with the ion core are very large compared to the weak interactions responsible for the hyperfine structure. It thus appears surprising, at first sight, that a collision approach such as MQDT should be at all successful in providing a detailed

description of the hyperfine structure of Rydberg states. A closer inspection, however, reveals that it is precisely the many orders of magnitude difference, in the close-coupling region, between the hyperfine interaction (at most a few gigahertz, but typically less) and other interactions such as the spin-orbit or the exchange interactions (typically  $10^4$  GHz, sometimes even more) which lie at the origin of the power of MQDT to treat the hyperfine structure in Rydberg states: The hyperfine interactions have an almost completely negligible effect on the close-coupling parameters (eigen quantum defects  $\mu_\alpha$ , channel coupling parameters, etc.) used by MQDT.

In the long-range part of the electron-ion collision, where the electron is completely decoupled from the ion core, however, the hyperfine interaction strongly affects the energy level structure but corresponds primarily to that of the ionic core. Two conclusions can immediately be drawn from these remarks and form the basis of the MQDT model developed in the present work.

(1) When the Rydberg level structure of an atom with an  $I=0$  nuclear spin is well described by a set of close-coupling MQDT parameters, this set of MQDT parameters can be employed without changes to treat the hyperfine structure of any  $I>0$  isotope of the same atom. The number of channels, however, must be enlarged, and identical close-coupling parameters must be assigned to all channels that differ only in the total angular momentum quantum number  $F$ .

(2) The origin of the hyperfine structure splittings in all Rydberg states, regardless of the value of  $n$ , must be sought in the hyperfine structure of the ion. Consequently, the hyperfine structure in Rydberg states need only be parametrized in terms of the ionic hyperfine structure rather than by separate hyperfine structure coupling constants for the successive members of the Rydberg series.

Although the nuclear spins have a negligible effect on the close-coupling parameters, they have a profound effect on the appearance of Rydberg state spectra, particularly at high  $n$  values. These effects are twofold. First, since  $J$  ceases to be a good quantum number when the effects of the nuclear spins are included, transitions that are strictly forbidden in  $I=0$  isotopes become weakly allowed. In the case of the rare-gas atoms examined here, transitions from the  $^1S_0$  ground state to Rydberg states that would have been classified as  $J=0$  or  $J=2-4$  states in the absence of nuclear spin become observable whenever the Rydberg states gain  $J=1$  character by the hyperfine interactions. Second, at sufficiently high  $n$  values, the ionic hyperfine structure intervals inevitably become comparable to the  $2R/n^3$  intervals between adjacent Rydberg states and obscure the regular appearance of the Rydberg series.

As will be shown in the following sections, a MQDT analysis of the hyperfine structure of the rare-gas atoms reduces the need to determine hyperfine coupling constants for each Rydberg level and leads to an adequate, although approximate, parametrization solely in terms of the hyperfine coupling constants of the ion. In addition, the hyperfine structure of the Rydberg states represents a very stringent test of the quality of MQDT parameters and may provide a way to extract precious information on the  $s$ - $d$  interaction in the rare gases and on the ionic hyperfine structure.

This article is structured as follows. Section II provides a short description of our experimental procedure. The well-known 16-channel QDT treatment of the  $s$  and  $d$  ( $J=0-4$ ) channels of the  $I=0$  isotopes of the rare-gas atoms and its extension to a 44-channel QDT treatment that includes the effects of the  $I=9/2$  nuclear spin of  $^{83}\text{Kr}$  are presented in Sec. III. The experimental results for the hyperfine structure of  $ns$  and  $nd$  Rydberg states are compared with MQDT calculations in Sec. IV, in which we also explain how MQDT parameters and the hyperfine structure of  $^{83}\text{Kr}^+$  were extracted from the experimental data in a nonlinear least-squares-fit procedure. Section V provides a discussion of the applicability of the present model to studying Rydberg states over a wide range of  $n$  values and of its use in future determinations of the  $s$ - $d$  interaction in the Rydberg spectrum of Kr and other rare gases.

## II. EXPERIMENT

The spectra were recorded using a narrow-bandwidth ( $0.008\text{ cm}^{-1}$ ) VUV laser system coupled to a photoion or photoelectron time-of-flight (TOF) mass spectrometer. The main aspects of our experimental procedure have been described in detail earlier [25,50] and are only briefly summarized here.

VUV radiation is generated by two-photon resonance-enhanced sum-frequency mixing ( $\nu_{\text{VUV}}=2\nu_1+\nu_2$ ) in Kr using the  $(4p)^55p'[1/2]_0\leftarrow(4p)^61S_0$  two-photon resonance at  $2\bar{\nu}_1=98\,855.1\text{ cm}^{-1}$ . To achieve a near-Fourier-transform-limited VUV bandwidth, two pulse-amplified cw ring dye lasers are used as input beams to the nonlinear frequency up-conversion processes. The VUV radiation is separated from the fundamental beams in a vacuum monochromator. The separation is achieved by a toroidal dispersion grating which also recollimates the diverging VUV beam and redirects it toward a photoexcitation or photoionization chamber equipped with a linear TOF mass spectrometer. The VUV wave number is calibrated to an absolute accuracy of  $0.015\text{ cm}^{-1}$  following the procedure described in Ref. [25], which involves the stabilization of the wave number of the first laser.

Krypton gas (Pangas, spectroscopic grade purity) is used without further purification and is introduced into the spectrometer in a pulsed skimmed supersonic expansion. The krypton gas jet is crossed at a right angle by the VUV laser beam in the middle of an array of resistively coupled cylindrical extraction plates. The photoexcitation region and the TOF mass spectrometer are surrounded by a double layer of  $\mu$ -metal shielding. The stray electric fields are measured and reduced to below  $2\text{ mV/cm}$  following the procedure described in Ref. [49]. Under the experimental conditions used to record the spectra of the high Rydberg states of krypton, pressure shifts and dc and ac Stark shifts are negligible for the Rydberg states with principal quantum number between 30 and 150 used in the MQDT analysis. Most lines have a full width at half maximum of  $0.01\text{ cm}^{-1}$ , which is slightly broader than the bandwidth of the VUV laser, presumably because of a residual Doppler broadening.

Spectra of the Rydberg states located below the  $^2P_{3/2}$  ion-

ization threshold are recorded by monitoring the pulsed-field ionization yield as a function of the VUV wave number. The pulsed electric field of up to  $1000\text{ V/cm}$  was applied  $1\text{ }\mu\text{s}$  after the VUV laser pulse, so that photoexcitation could take place under field-free conditions. The pulsed electric field also served the purpose of extracting the  $\text{Kr}^+$  ions toward a microchannel plate detector at the end of the TOF tube. Spectra of the different isotopes were obtained by placing temporal gates at the corresponding positions in the TOF spectrum. The  $1000\text{ V/cm}$  magnitude of the pulsed electric field implies that pulsed-field ionization is observable down to about  $200\text{ cm}^{-1}$  below the  $^2P_{3/2}$  field-free ionization threshold and that Rydberg states above  $n\approx 25$  can be detected. To detect transitions to Rydberg states of lower  $n$  values, the krypton atoms were ionized with the  $532\text{ nm}$  radiation of a neodymium-doped yttrium aluminum garnet (Nd:YAG) laser.

## III. MQDT OF THE HYPERFINE STRUCTURE OF RYDBERG STATES OF KRYPTON

To analyze the Rydberg spectrum of  $^{83}\text{Kr}$  using MQDT we follow the formalism introduced by Lu [6] and Lee and Lu [36] in their study of the single-photon VUV photoabsorption and photoionization spectra of Xe and Ar, which consist of transitions to odd-parity  $\ell=0$  and  $2$  channels with  $J=1$ . Their formalism was applied by Aymar and co-workers [34] to treat the  $J=0-4$  odd-parity bound Rydberg states of Kr. After a brief review of this formalism in Sec. III A, we describe how it was extended to treat the hyperfine structure in  $^{83}\text{Kr}$  in Sec. III B.

### A. MQDT for the $I=0$ isotopes of Kr

The MQDT formalism of Refs. [6,34,36] provides an accurate description of the Rydberg spectra of the  $I=0$  isotopes of the rare-gas atoms. It allows the calculation of line shapes, line positions, and spectral intensities in terms of a set of close-coupling parameters consisting of (1) the eigen quantum defects  $\mu_\alpha$ , (2) the elements  $U_{i\alpha}$  of the transformation matrix between the close-coupling eigenchannels  $\alpha$  and the dissociation channels  $i$ , (3) the dipole amplitudes  $D_\alpha$  for the transitions to the eigenchannels, and (4) the positions of the ionization thresholds. Whereas the dissociation channels are  $jj$  coupled, the close-coupling eigenchannels are almost perfectly described by  $LS$  coupling. Table I summarizes the notation generally used to designate both sets of channels. A total of 16 channels must be retained for the treatment of the  $s$  and  $d$  Rydberg series associated with the  $^2P$  ground state of the ion: two channels with  $J=0$ , five with  $J=1$ , five with  $J=2$ , three with  $J=3$ , and one with  $J=4$ .

The elements  $U_{i\alpha}$  of the transformation matrix are conveniently factorized as

$$U_{i\alpha} = \sum_{\bar{\alpha}} U_{i\bar{\alpha}} V_{\bar{\alpha}\alpha}, \quad (1)$$

where the  $U_{i\bar{\alpha}}$  elements represent elements of the  $jj$ - $LS$  transformation matrix and  $V_{\bar{\alpha}\alpha}$  accounts for the (typically very small) departure of the close-coupling eigenchannels from

TABLE I. Overview of the notation and the quantum numbers used to designate the close-coupling eigenchannels and the dissociation channels in the MQDT treatment of the  $s$  and  $d$  Rydberg series of Kr converging to the  $^2P$  ground state of  $\text{Kr}^+$ .

$J$	$\ell$	Close-coupling channels			Dissociation channels		
		Notation	$L$	$S$	Notation	$J^+$	$j$
0	0	$(p^5s)^3P_0$	1	1	$(^2P_{1/2})s_{1/2}$	1/2	1/2
	2	$(p^5d)^3P_0$	1	1	$(^2P_{3/2})d_{3/2}$	3/2	3/2
1	0	$(p^5s)^1P_1$	1	0	$(^2P_{1/2})s_{1/2}$	1/2	1/2
	0	$(p^5s)^3P_1$	1	1	$(^2P_{3/2})s_{1/2}$	3/2	1/2
	2	$(p^5d)^1P_1$	1	0	$(^2P_{1/2})d_{3/2}$	1/2	3/2
	2	$(p^5d)^3P_1$	1	1	$(^2P_{3/2})d_{3/2}$	3/2	3/2
2	0	$(p^5s)^3D_1$	2	1	$(^2P_{3/2})d_{5/2}$	3/2	5/2
	2	$(p^5s)^3P_2$	1	1	$(^2P_{3/2})s_{1/2}$	3/2	1/2
	2	$(p^5d)^3P_2$	1	1	$(^2P_{1/2})d_{3/2}$	1/2	3/2
	2	$(p^5d)^1D_2$	2	0	$(^2P_{1/2})d_{5/2}$	1/2	5/2
3	2	$(p^5d)^3D_2$	2	1	$(^2P_{3/2})d_{3/2}$	3/2	3/2
	2	$(p^5d)^3F_2$	3	1	$(^2P_{3/2})d_{5/2}$	3/2	5/2
	2	$(p^5s)^3D_3$	2	1	$(^2P_{1/2})d_{5/2}$	1/2	5/2
	2	$(p^5d)^1F_3$	3	0	$(^2P_{3/2})d_{3/2}$	3/2	3/2
4	2	$(p^5d)^3F_3$	3	1	$(^2P_{3/2})d_{5/2}$	3/2	5/2
	2	$(p^5d)^3F_4$	3	1	$(^2P_{3/2})d_{5/2}$	3/2	5/2

pure  $LS$  coupling and the resulting channel mixings, in particular the mixing between  $s$  and  $d$  channels.  $V_{\bar{\alpha}\alpha}$  can be represented in terms of generalized Euler angles [36]. Because  $J$  is a good quantum number, the  $U_{i\alpha}$  and  $V_{\bar{\alpha}\alpha}$  matrices have a block-diagonal structure with a  $(2 \times 2)$   $J=0$ , a  $(5 \times 5)$   $J=1$ , a  $(5 \times 5)$   $J=2$ , a  $(3 \times 3)$   $J=3$ , and a  $(1 \times 1)$   $J=4$  block.

The MQDT parameters can be derived from experimental spectra of the bound Rydberg states semiempirically. Each bound energy level is used to derive two effective principal quantum numbers  $\nu_{3/2}$  and  $\nu_{1/2}$  defined by the relations

$$E = E(^2P_{1/2}) - \frac{R_M}{\nu_{1/2}^2} = E(^2P_{3/2}) - \frac{R_M}{\nu_{3/2}^2}, \quad (2)$$

where  $E(^2P_{J^+})$  with  $J^+ = 1/2, 3/2$  represent the ionization energies corresponding to the formation of the two spin-orbit components of the  $\text{Kr}^+$  ion, and  $R_M$  stands for the mass-dependent Rydberg constant.

In the discrete part of the spectrum, a second equation,

$$\sum_{\alpha} U_{i\alpha} \sin[\pi(\mu_{\alpha} + \nu_{J^+})] A_{\alpha} = 0, \quad (3)$$

which requires the wave functions of the bound levels to vanish at infinity, is used jointly with Eq. (2) to determine their positions for a given set of MQDT parameters. The coefficients  $A_{\alpha}$  enable the expansion of the dissociation channels in the basis of the close-coupling eigenchannels. The bound states of the electron-ion-core system correspond to the binding energies  $-R_M/\nu_{J^+}^2$  for which Eq. (3) has no trivial solution, i.e., the energies that satisfy the relation

$$\det|U_{i\alpha} \sin[\pi(\mu_{\alpha} + \nu_{J^+})]| = 0. \quad (4)$$

The intensities  $\mathcal{I}$  of the transitions from the ground state to the bound Rydberg levels can be calculated from the dipole amplitudes  $D_{\alpha}$  and the expansion coefficients  $A_{\alpha}$  according to

$$\mathcal{I} \propto \left( \sum_{\alpha} D_{\alpha} A_{\alpha} \right)^2, \quad (5)$$

where  $D_{\alpha}$  can be expressed as a linear combination of dipole amplitudes to purely  $LS$ -coupled channels,

$$D_{\alpha} = \sum_{\bar{\alpha}} V_{\bar{\alpha}\alpha}^* D_{\bar{\alpha}}, \quad (6)$$

The MQDT parameters can either be evaluated *ab initio* [37] or derived from experimental data in a least-squares-fit procedure [34]. Assuming that the energy dependence of the MQDT parameters  $\mu_{\alpha}$  and  $V_{\bar{\alpha}\alpha}$  is only weak and can therefore be adequately described by the linear relations

$$\mu_{\alpha} = \mu_{\alpha}^{(0)} + \epsilon \mu_{\alpha}^{(1)} \quad \text{with} \quad \epsilon = 1/\nu_{3/2}^2 \quad (7)$$

and

$$V_{\bar{\alpha}\alpha} = V_{\bar{\alpha}\alpha}^{(0)} + \epsilon V_{\bar{\alpha}\alpha}^{(1)} \quad \text{with} \quad \epsilon = 1/\nu_{3/2}^2 \quad (8)$$

leads to a number of MQDT parameters often too large to be determined from experimental data. A reduction of the number of parameters to be determined in a least-squares fit can be achieved by making the approximation that the close-coupling eigenchannels are exactly  $LS$  coupled, in which case the elements  $U_{i\alpha}$  of the transformation matrix become identical to the elements  $U_{i\bar{\alpha}}$  of the well-known  $jj$ - $LS$  transformation matrix, by neglecting the energy dependence of certain parameters, or by fixing their values to values determined previously.

Several sets of  $V_{\bar{\alpha}\alpha}$  elements (or of the corresponding mixing angles) and of close-coupling eigenchannel quantum defects  $\mu_{\alpha}$  have been determined in previous studies of the Rydberg spectrum of Kr [32,34,37]. Aymer *et al.* [34] compared their transformation matrix  $U_{i\alpha}$  for the  $J=1$  channels with previous results by Johnson *et al.* [37] and Geiger [32], and have also derived the complete transformation matrices for  $J=0-3$ . From these data, the matrix elements  $V_{\bar{\alpha}\alpha}$  can be determined for each value of  $J$  using Eq. (9):

$$V_{\bar{\alpha}\alpha} = \sum_i U_{\bar{\alpha}i}^* U_{i\alpha}. \quad (9)$$

The different sets of  $V_{\bar{\alpha}\alpha}$  parameters that can be extracted from the literature on Kr differ markedly, in both sign and magnitude. Inspection of the available data on channel interactions in the rare gases [34,36,39,41] leads to the conclusions that (a) the magnitude of the  $V_{\bar{\alpha}\alpha}$  elements (or of the mixing angles) increases in the sequence Ne, Ar, Xe although the mixing angles reported for Kr appear to be larger than those of Xe, and (b) the discrepancies in the values reported for Kr by different authors are likely to originate from the

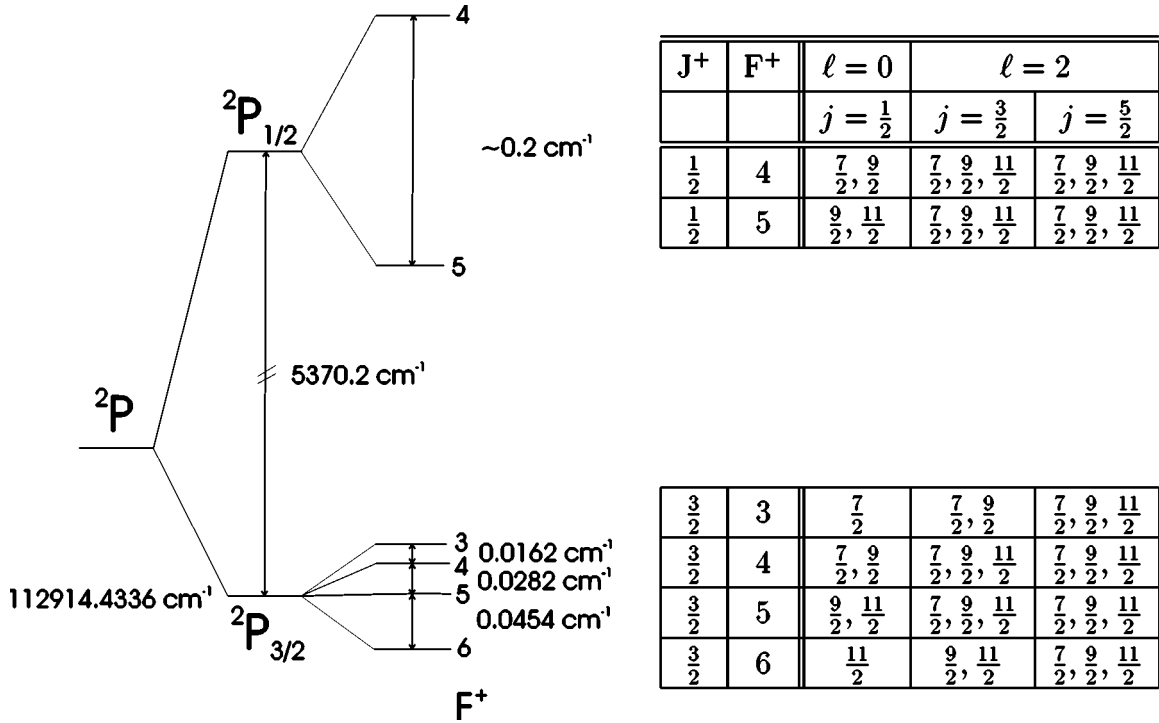


FIG. 1. Schematic diagram (not to scale) of the hyperfine structure in the  $^2P_{3/2}$  and  $^2P_{1/2}$  spin-orbit components of  $^{83}\text{Kr}^+$ . The total angular momentum quantum number  $F$  of the  $s$  and  $d$  dissociation channels associated with each hyperfine structure component is tabulated on the right-hand side of the figure. The numerical values given for the hyperfine structure intervals correspond to the results of the MQDT analysis.

fact that either they were derived from measurements in different energetic regions, or the energy dependence of the MQDT parameters was taken into account differently. In the analysis presented in Sec. IV we used the energy dependences of the MQDT parameters reported by Aymar and co-workers [34] and did not attempt to refine them.

### B. MQDT for $^{83}\text{Kr}$

The 16-channel MQDT analysis of the  $s$  and  $d$  series of the  $I=0$  isotopes of Kr outlined above can be extended to include the nuclear spin ( $I=9/2$ ) of the  $^{83}\text{Kr}$  nucleus if one assumes that the effect of the hyperfine interactions on the values of the close-coupling eigen quantum defects is negligible compared to that of the exchange and spin-orbit interactions. Consequently,  $J$  remains a good quantum number in the close-coupling region, and the number of channels for  $^{83}\text{Kr}$  is readily obtained by considering the possible total angular momentum vectors that result from the addition of  $\vec{J}$  and  $\vec{I}$ . The following angular momentum coupling hierarchy provides an adequate description of the close-coupling eigenchannels:

$$\vec{L}^+ + \vec{\ell} = \vec{L}, \quad \vec{S}^+ + \vec{s} = \vec{S}, \quad \vec{L} + \vec{S} = \vec{J}, \quad \vec{J} + \vec{I} = \vec{F}, \quad (10)$$

where  $\vec{L}^+$  and  $\vec{S}^+$  represent the orbital and spin angular momenta of the ionic core,  $\vec{\ell}$  and  $\vec{s}$  the corresponding angular momenta of the Rydberg electron, and  $\vec{I}$  the nuclear spin. When treating the single-photon photoabsorption and photo-

ionization spectra recorded following excitation from the  $^1S_0$  ( $F=9/2$ ) ground state of  $^{83}\text{Kr}$ , the  $\Delta F=0, \pm 1$  ( $0 \leftrightarrow 0$ ) electric dipole selection rule restricts the number of channels to three (degenerate) hyperfine components with  $F=7/2, 9/2$ , and  $11/2$  for each eigenchannel with  $J \geq 1$ , and to a single component with  $F=9/2$  for the  $J=0$  eigenchannels. A total of 44 eigenchannels results, comprising 10  $s$  channels ( $\ell=0$ ) and 34  $d$  channels ( $\ell=2$ ).

The dissociation channels can be described by the following angular momentum coupling scheme:

$$\vec{L}^+ + \vec{S}^+ = \vec{J}^+, \quad \vec{J}^+ + \vec{I} = \vec{F}^+, \quad \vec{\ell} + \vec{s} = \vec{j}, \quad \vec{F}^+ + \vec{j} = \vec{F}, \quad (11)$$

where  $\vec{J}^+$  and  $\vec{F}^+$  represent the electronic and total angular momenta of the ionic core. The dominant interaction in the ionic core is the spin-orbit coupling, which leads to an energy splitting of  $5370.2 \text{ cm}^{-1}$  between the  $^2P_{3/2}$  and  $^2P_{1/2}$  levels, several orders of magnitude larger than the splittings induced by the hyperfine interactions. Under the assumption that the mixing of the  $^2P_{3/2}$  and  $^2P_{1/2}$  spin-orbit components of the ion by the hyperfine interactions is negligible (such a mixing is in principle possible for states with  $F^+=4,5$  but is expected to be extremely weak because of the large energy separation between the two spin-orbit components), the hyperfine structure of the two spin-orbit components can be treated separately and expressed as a function of the magnetic dipole and electric quadrupole hyperfine constants  $A_{J^+}$  and  $B_{J^+}$  [51] ( $B_{J^+=1/2}=0$  for the  $^2P_{1/2}$  spin-orbit level):

$$\begin{aligned} \tilde{\nu}(J^+, F^+) = & \tilde{\nu}_{J^+} + A_{J^+} \frac{C}{2} \\ & + B_{J^+} \frac{\frac{3}{4}C(C+1) - I(I+1)J^+(J^++1)}{2I(2I-1)J^+(2J^+-1)}, \end{aligned} \quad (12)$$

where

$$C = F^+(F^++1) - I(I+1) - J^+(J^++1). \quad (13)$$

In Eq. (12),  $\tilde{\nu}_{J^+}$  represents the energy of the center of gravity of the hyperfine structure of the two spin-orbit components ( $J^+ = 1/2, 3/2$ ). The dissociation channels are hence characterized by a pair of intermediate quantum numbers  $J^+$  and  $F^+$  designating each ionization threshold. The left-hand side of Fig. 1 displays schematically the energy level structure of the  $^{83}\text{Kr}^+$  ion, which consists of six hyperfine components forming a group of four levels at the  $^2P_{3/2}$  threshold and a group of two levels at the  $^2P_{1/2}$  threshold. The total number of dissociation channels to be retained in the treatment of the single-photon photoabsorption and photoionization spectra can be determined as above for the close-coupling eigenchannels by considering the restrictions imposed by the  $\Delta F = 0, \pm 1$  ( $0 \leftrightarrow 0$ ) electric dipole selection rule. All dissociation channels are listed on the right-hand side of Fig. 1. For the  $s$  states ( $\ell = 0, j = 1/2$ ) two channels result for each ionic state with  $F^+ = 4$  and 5, whereas only one channel is associated with the  $F^+ = 3$  and 6 ionic states, resulting in a total of 10  $s$  channels. Analogous considerations lead to the identification of 34  $d$  channels ( $\ell = 2, j = 3/2$  and  $5/2$ ).

The semiempirical MQDT treatment outlined in the previous subsection can be adapted to treat the hyperfine structure of the Rydberg states of  $^{83}\text{Kr}$ , given the following.

(1) The close-coupling MQDT parameters are taken over without change from the treatment of the  $I=0$  isotopes, but the number of channels is enlarged from 16 to 44, identical close-coupling parameters being assigned to all channels that differ only in the total angular momentum quantum number  $F$ .

(2) Equation (2) is generalized to include a set of six effective principal quantum numbers  $\nu_{J^+F^+}$  defined relative to the position of each of the six ionization thresholds depicted in Fig. 1:

$$E = E(^2P_{J^+F^+}) - \frac{R_M}{\nu_{J^+F^+}^2}. \quad (14)$$

(3) The transformation matrix  $U_{i\alpha}$  is extended from a 16- to a 44-channel situation. This extension necessitates an additional label for the quantum number  $F$ , and we denote the elements of the extended transformation matrix  $U_{i_F\alpha_F}$ .

Because the close-coupling MQDT parameters are not affected by the hyperfine interactions in our model, the elements of the transformation matrix can be factorized as in Eq. (1) above:

$$U_{i_F\alpha_F} = \sum_{\bar{\alpha}_F} U_{i_F\bar{\alpha}_F} V_{\bar{\alpha}_F\alpha_F}. \quad (15)$$

To convert the matrix  $V_{\bar{\alpha}\alpha}$  into a  $44 \times 44$   $V_{\bar{\alpha}_F\alpha_F}$  matrix, care has to be taken to couple only manifolds with equal  $F$  values. Standard angular momentum algebra [52] can be used to derive the angular momentum transformation  $U_{i_F\bar{\alpha}_F}$

$$U_{i_F\bar{\alpha}_F} = \langle LSJF | J^+ F^+ j F \rangle \quad (16)$$

between the  $LSJF$ -coupled eigenchannels and the  $J^+ F^+ j F$ -coupled dissociation channels

$$\begin{aligned} \langle LSJF | J^+ F^+ j F \rangle = & (2F+1) \sqrt{(2J+1)(2L+1)(2S+1)(2j+1)(2F^++1)(2J^++1)} \\ & \times \sum_{m_j, m_{J^+}, m_J, m_\ell, m_{L^+}, m_L, m_s, m_{S^+}, m_S, m_{F^+}, m_I} (-1)^{F^+ - j - J^+ + 2I - J + L - S - 2s + 3m_F + m_{J^+} + 2m_J + m_j} \\ & \times \begin{pmatrix} I & J & F \\ m_I & m_J & -m_F \end{pmatrix} \begin{pmatrix} L & S & J \\ m_L & m_S & -m_J \end{pmatrix} \begin{pmatrix} L^+ & \ell & L \\ m_{L^+} & m_\ell & -m_L \end{pmatrix} \begin{pmatrix} S^+ & s & S \\ m_{S^+} & m_s & -m_S \end{pmatrix} \\ & \times \begin{pmatrix} F^+ & j & F \\ m_{F^+} & m_j & -m_F \end{pmatrix} \begin{pmatrix} \ell & s & j \\ m_\ell & m_s & -m_j \end{pmatrix} \begin{pmatrix} I & J^+ & F^+ \\ m_I & m_{J^+} & -m_{F^+} \end{pmatrix} \begin{pmatrix} L^+ & S^+ & J^+ \\ m_{L^+} & m_{S^+} & -m_{J^+} \end{pmatrix}. \end{aligned} \quad (17)$$

The  $U_{i_F\bar{\alpha}_F}$  transformation has a block-diagonal structure. The  $s$  block consists of a  $(3 \times 3)$   $F=7/2$ , a  $(4 \times 4)$   $F=9/2$ , and a  $(3 \times 3)$   $F=11/2$  subblock, whereas the  $d$  block is composed of an  $(11 \times 11)$   $F=7/2$ , a  $(12 \times 12)$   $F=9/2$ , and an  $(11 \times 11)$   $F=11/2$  subblock. The elements of the  $U_{i_F\bar{\alpha}_F}$  matrix can be calculated numerically and the positions of the Rydberg levels determined from the condition

$$\sum_{\alpha_F} U_{i_F\alpha_F} \sin[\pi(\mu_{\alpha_F} + \nu_{J^+F^+})] A_{\alpha_F} = 0, \quad (18)$$

which has nontrivial solutions when

$$\det | U_{i_F\alpha_F} \sin[\pi(\mu_{\alpha_F} + \nu_{J^+F^+})] | = 0. \quad (19)$$

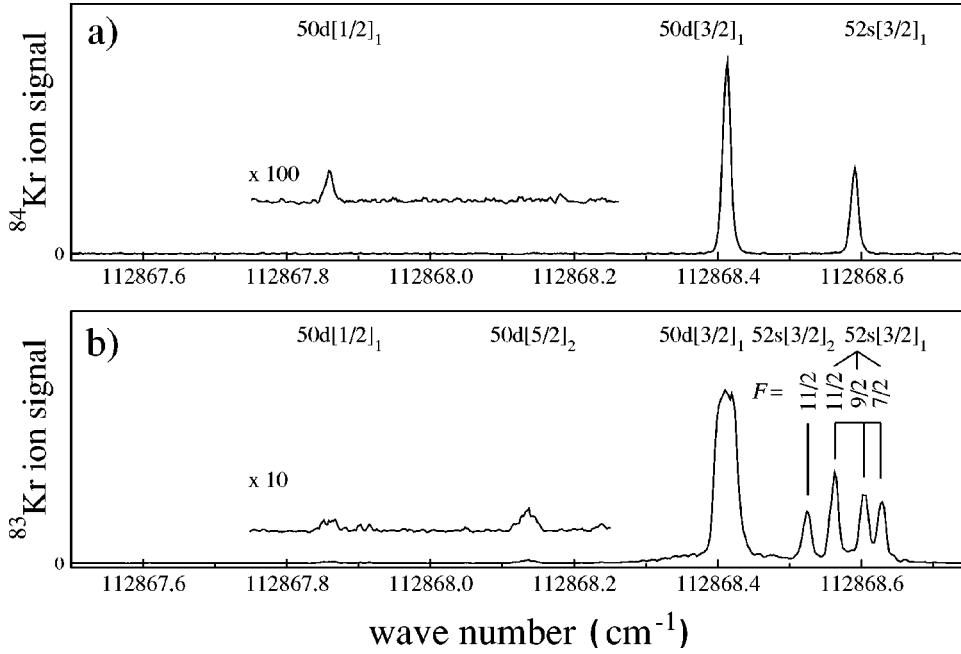


FIG. 2. Comparison of the pulsed-field ionization spectra of (a)  $^{84}\text{Kr}$  and (b)  $^{83}\text{Kr}$  in the region of effective principal quantum number  $\nu_{3/2}$  between 48 and 49 recorded following single-photon excitation from the  $^1S_0$  ground state. The hyperfine interaction leads to the splitting of the  $(n+2)s[3/2]_1$  Rydberg states into three components, the broadening of the transition to the  $nd[3/2]_1$  Rydberg state, the enhancement of the intensity of the transition to the  $nd[1/2]_1$  state, and the observation of additional structures at the positions of the  $J=2$  components of the  $(n+2)s$  and  $nd$  Rydberg states.

The general form of Eq. (19) is also adapted to a treatment neglecting the departure of the close-coupling eigenchannels from pure  $LS$  coupling, in which case the transformation matrix  $U_{i_F\alpha_F}$  must be replaced by the angular momentum transformation matrix  $U_{i_F\bar{\alpha}_F}$ .

The intensity of a transition from the ground state ( $^1S_0$ ,  $F=9/2$ ) to a Rydberg state is determined by the value of  $F$  and by the expansion coefficients  $A_{\alpha_F}$  of the total wave function of the target state in the basis of the close-coupled channels according to

$$\mathcal{I} \propto W_F \left( \sum_{\alpha_F} D_{\alpha_F} A_{\alpha_F} \right)^2. \quad (20)$$

The dipole amplitudes  $D_{\alpha_F}$  are approximated by the  $D_{\alpha}$  dipole amplitudes used in the MQDT treatment of the  $I=0$  isotopes. The weighting factors  $W_F$  are calculated according to Ref. [53] and satisfy the condition  $W_{11/2}:W_{9/2}:W_{7/2} = 1.2:1.0:0.8$ , which is in accordance with the multiplicity sum rules for electric dipole transitions.

#### IV. RESULTS

A comparison of the pulsed-field ionization spectra of  $^{83}\text{Kr}$  and  $^{84}\text{Kr}$  in the region of effective principal quantum number  $\nu_{3/2}=48-49$  is presented in Fig. 2. The spectra were recorded under identical experimental conditions, using a pulsed electric field of 100 V/cm applied 1  $\mu\text{s}$  after photoexcitation. The intensity distribution of the  $^{84}\text{Kr}$  spectrum [Fig. 2(a)] is dominated by the  $ns[3/2]_1$  and  $nd[3/2]_1$  series. The  $nd[1/2]_1$  series, which becomes visible only on an enlarged scale, is particularly weak in this region of the spectrum because of its dominant  $^3P_1$  character. Although the overall appearance of the  $^{83}\text{Kr}$  spectrum [Fig. 2(b)] is similar, several differences are noticeable. First, the  $ns[3/2]_1$  line is split into a well-resolved triplet and the  $nd[3/2]_1$  line ap-

pears broadened. Second, features that are not present in the  $^{84}\text{Kr}$  spectrum can be observed on the low-energy side of the  $ns[3/2]_1$  triplet and halfway between the positions of the transitions to the  $nd[3/2]_1$  and the  $nd[1/2]_1$  states.

These differences have their origin in the hyperfine interactions with the  $I=9/2$  nuclear spin of  $^{83}\text{Kr}$ , which leads to additional splittings in the energy level structure and induces sufficient  $J$  mixing that Rydberg states which would be classified as  $J=2$  states in the  $I=0$  isotopes become accessible in single-photon transitions from the  $^1S_0$  ground state. Although available MQDT parameters, in particular those reported by Aymar *et al.* [34], have been an invaluable help to our initial progress in the understanding of the  $^{83}\text{Kr}$  spectrum, they turned out not to be accurate enough for the quantitative modeling of the spectrum of the  $^{83}\text{Kr}$  isotope.

In order to be able to test the fundamental assumption of our MQDT model, namely, that the same close-coupling MQDT parameters can be used to calculate the spectra of both isotopes, our analysis was carried out in two steps. First, the  $^{84}\text{Kr}$  spectrum was used to derive a set of MQDT parameters accurate enough to provide a quantitative description of the  $J=1$  series in the energetic region investigated, i.e., between 112 800 and 112 905  $\text{cm}^{-1}$ . Then, this parameter set was kept fixed and used in the analysis of the  $^{83}\text{Kr}$  spectrum. The first step of the analysis is summarized in Sec. IV A and the second in Sec. IV B.

##### A. $^{84}\text{Kr}$

For the analysis of the  $^{84}\text{Kr}$  isotope, a set of 187 wave numbers corresponding to transitions to members of the  $ns[3/2]_1$  series between  $n=33$  and 115, of the  $nd[3/2]_1$  series between  $n=31$  and 113, and of the  $nd[1/2]_1$  series between  $n=32$  and 52 was used. The transition wave numbers were determined with an absolute accuracy of 0.015  $\text{cm}^{-1}$  and their relative positions with an accuracy of 0.008  $\text{cm}^{-1}$ . These wave numbers, which are available as supplementary

TABLE II. Eigen quantum defects and ionization energy (IE) of  $^{84}\text{Kr}$  determined from a nonlinear least-squares fit based on 187 experimental spectral positions of members of the  $ns[3/2]_1$ ,  $nd[3/2]_1$ , and  $nd[1/2]_1$  series with  $n$  between 31 and 115. The values given in parentheses represent one standard deviation ( $1\sigma$ ). In the MQDT calculations, the energy dependence of the MQDT parameters was kept fixed at the values of Ref. [34]. RMSD represents the root-mean-square deviation of the fit.

Eigenchannel	$\mu_\alpha^{(0)}$ from Ref. [34]	$\mu_\alpha^{(1)}$ from Ref. [34]	$\mu_\alpha^{(0)}$ fitted with $U_{i\bar{\alpha}}^a$	$\mu_\alpha^{(0)}$ fitted with $U_{i\alpha}^a$
$(p^5d)^1P_1$	0.0941	0.075	0.09480(46)	0.09437(32)
$(p^5d)^3P_1$	0.4725	-0.516	0.4703(1)	0.4692(1)
$(p^5d)^3D_1$	0.2572	-0.818	0.2550(4)	0.2523(3)
$(p^5s)^1P_1$	0.0626	0.103	0.05802(20)	0.05757(20)
$(p^5s)^3P_1$	0.1126	0.238	0.1099(3)	0.1103(4)
IE ( $^{84}\text{Kr}$ ) ( $\text{cm}^{-1}$ )	112 914.434(15) <sup>b</sup>		112 914.4357(1) <sup>c</sup>	112 914.4356(1) <sup>c</sup>
RMSD ( $\text{cm}^{-1}$ )			$3.69 \times 10^{-3}$	$3.64 \times 10^{-3}$

<sup>a</sup>The energy dependence  $\mu_\alpha^{(1)}$  of Ref. [34] (third column) was held fixed in the present work.

<sup>b</sup>From Ref. [25].

<sup>c</sup>The uncertainty represents  $1\sigma$  in the fit and does not include the  $0.015 \text{ cm}^{-1}$  uncertainty in the VUV calibration.

material [54], were then used in a nonlinear least-squares-fit procedure based on the MQDT model described in Sec. III A. Because our data set covered only a narrow energy range, no attempt was made to refine the values of the energy dependence of the MQDT parameters. Originally, we intended to fit some of the elements of the  $V_{\bar{\alpha}\alpha}$  matrix. However, after it turned out that these elements cannot be determined from our data set, two types of fits were carried out to determine the eigen quantum defects  $\mu_\alpha^{(0)}$  and the  $^2P_{3/2}$  ionization threshold, one in which the  $U_{i\alpha}$  matrix reported by Aymar *et al.* [34] was used, the other in which the  $V_{\bar{\alpha}\alpha}$  matrix was set to unity.

Table II compares the MQDT parameters determined in both fits. Surprisingly, the fit based on the  $U_{i\alpha}$  transformation matrix did not lead to a significantly smaller root-mean-square deviation (RMSD) than the fit based on the approximate  $U_{i\bar{\alpha}}$  transformation.

The following conclusions can be drawn from the MQDT analysis of the Rydberg spectrum of  $^{84}\text{Kr}$ .

(1) MQDT parameters available in the literature, while entirely adequate to describe earlier experimental data recorded at lower resolution, had to be slightly modified to account for the line positions determined in our high-resolution study. The only eigen quantum defect that was found to differ significantly from the results of Aymar *et al.* [34] is that of the  $(p^5s)^1P_1$  channel (see Table II). A satisfactory description of the relative intensities was reached by assuming zero values for the dipole amplitudes to the triplet channels and a ratio  $D_{\alpha=(p^5d)^1P_1}/D_{\alpha=(p^5s)^1P_1} = 1.5$  for the dipole amplitudes to the singlet channels.

(2) The simplified MQDT analysis based on the  $jj$ - $LS$  angular momentum frame transformation matrix  $U_{i\bar{\alpha}}$  gave an equally satisfactory description of our experimental data to that based on the  $U_{i\alpha}$  transformation matrix reported by Aymar *et al.* [34]. The eigen quantum defects extracted from both analyses are very similar, and the positions of the  $nd[3/2]_1$ ,  $nd[1/2]_1$ , and  $ns[3/2]_1$  series at high  $n$  values ( $n \geq 30$ ) do not contain sufficient information to determine the  $V_{\bar{\alpha}\alpha}$  matrix elements.

(3) To determine the  $V_{\bar{\alpha}\alpha}$  matrix elements, the inclusion of the positions of low- $n$  states in the MQDT analysis appears mandatory. However, when such states are included, one must also explicitly consider the energy dependence of the  $V_{\bar{\alpha}\alpha}$  matrix elements and of the eigen quantum defects by retaining a linear term in the former case and both a linear and a quadratic term in the latter case. Available data on the  $s$  and  $d$  Rydberg states of  $^{84}\text{Kr}$  are insufficient to extract statistically meaningful values for all these parameters, and our attempts at obtaining a fully satisfactory set of MQDT parameters over the entire range from  $n=5$  to the  $^2P_{3/2}$  threshold have remained unsuccessful.

Both parameter sets summarized in Table II will be shown in the next subsection to be adequate to describe the hyperfine structure in the Rydberg spectrum of  $^{83}\text{Kr}$  also. The spectrum of  $^{83}\text{Kr}$ , however, contains information that is helpful in determining MQDT parameters for the  $J \neq 1$  channels and thus in obtaining a more global description of the  $s$  and  $d$  Rydberg states of krypton, as explained below.

## B. $^{83}\text{Kr}$

Figure 3 shows an overview of the spectrum of the  $s$  and  $d$  Rydberg states of  $^{83}\text{Kr}$  in the ranges of effective principal quantum number  $\nu_{3/2} = 30.5-31$ ,  $40.5-41$ ,  $50.5-51$ , and  $60.5-61$ . The use of an effective quantum number scale rather than a wave number scale facilitates the recognition of the evolution of the spectral structures as  $n$  increases. Around  $n=30$ , the main differences from the spectrum of  $^{84}\text{Kr}$  are the splitting of the  $ns[3/2]_1$  line into a triplet with  $F=7/2$ ,  $9/2$ , and  $11/2$  and the broadening of the  $nd[3/2]_1$  resonance. The  $J$  mixing induced by the hyperfine interactions is hardly noticeable and leads to the additional groups of lines associated with transitions to the  $34s[3/2]_2$ ,  $32d[3/2]_2$ ,  $32d[5/2]_2$ ,  $32d[5/2]_3$ , and  $32d[7/2]_3$  Rydberg states that can be discerned only on an enlarged scale or at higher  $n$  values.

At increasing  $n$  values, the  $J=2$  and  $3$  components gradually gain in intensity, primarily because the spacings between the  $J=1$  and  $J \neq 1$  components that are coupled by the hy-

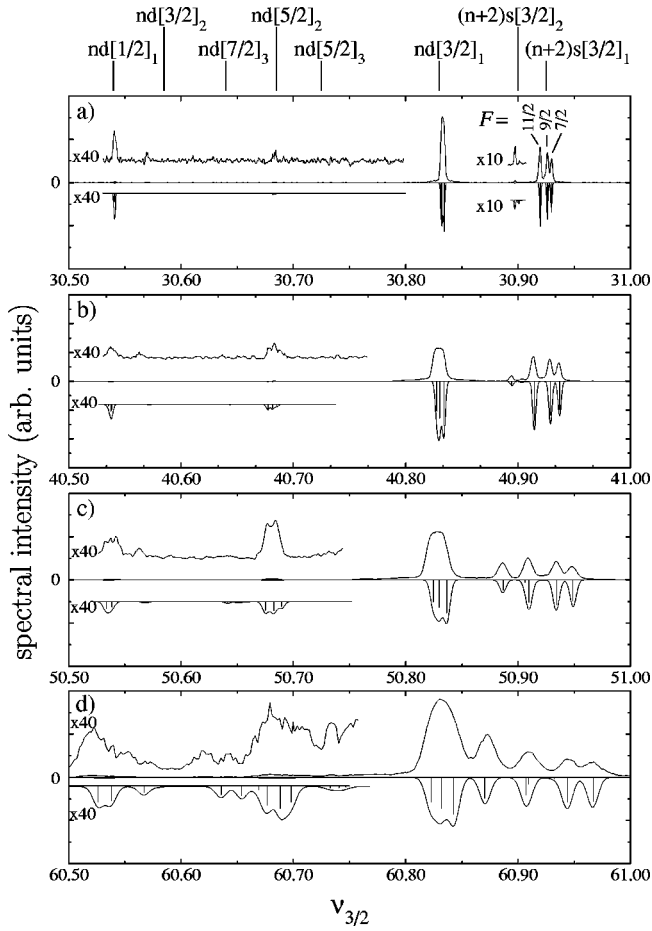


FIG. 3. Comparison of the hyperfine structure in experimental spectra and MQDT simulations (inverted traces and stick spectra) of  $s$  and  $d$  Rydberg states of  $^{83}\text{Kr}$  corresponding to single-photon excitation from the  $^1S_0$  ground state. For direct comparison of the hyperfine structure at different  $n$  values, the spectra are displayed as a function of the effective principal quantum number  $\nu_{3/2}$  defined with respect to the center of gravity of the hyperfine structure of the  $^2P_{3/2}$  ground state of  $^{83}\text{Kr}^+$ .  $\nu_{3/2} =$  (a) 30.5–31; (b) 40.5–41; (c) 50.5–51; (d) 60.5–61.

perfine interactions scale as  $n^{-3}$  whereas the dominant contributions to the hyperfine interactions, the interactions between  $\vec{J}^+$  and  $\vec{I}$ , are independent of  $n$ . Particularly striking is the evolution of the  $(n+2)s[3/2]_2$  components, which rapidly become as intense as the  $(n+2)s[3/2]_1$  components, and even stronger as they approach the  $nd[3/2]_1$  components. This evolution can be attributed to the  $s$ - $d$  interaction and will be discussed further in Sec. V C.

Only a subset of all observed features, namely, those corresponding to  $ns$  Rydberg states, display a fully resolved hyperfine structure that could be used in a least-squares fit of the hyperfine structure of the  $^{83}\text{Kr}^+$   $^2P_{3/2}$  ground state. The corresponding spectral positions are listed with their assignments in a table available as supplementary material [55].

Given that a similar agreement between theoretical predictions and experiment was reached using either the  $U_{i_F\alpha_F}$  or the  $U_{i_F\bar{\alpha}_F}$  transformation, only the results obtained with the  $U_{i_F\bar{\alpha}_F}$  transformation are presented here. The MQDT

TABLE III. Ionization energy of  $^{83}\text{Kr}$ , hyperfine coupling constants  $A_{J^+=3/2}$  and  $B_{J^+=3/2}$  of the  $^2P_{3/2}$  ground and  $A_{J^+=1/2}$  of the  $^2P_{1/2}$  excited state of  $^{83}\text{Kr}^+$ , and quantum defects for the  $^1D_2$ ,  $^3D_2$ , and  $^3F_2$ , eigenchannels of Kr determined in a least-squares-fit procedure based on the experimental positions of the hyperfine and fine structure components of the  $ns$  and  $nd$  Rydberg states. RMSD represents the root-mean-square deviation of the fit.

		This work
$A_{J^+=1/2}$ ( $\text{cm}^{-1}$ )		$\approx -0.04$
$A_{J^+=3/2}$ ( $\text{cm}^{-1}$ )	$-0.00619^a$	$-0.00616(4)$
$B_{J^+=3/2}$ ( $\text{cm}^{-1}$ )	$-0.0138^a$	$-0.0127(4)$
IE ( $^{83}\text{Kr}$ ) ( $\text{cm}^{-1}$ )		$112\,914.4336(8)^b$
RMSD ( $\text{cm}^{-1}$ )		$3.6 \times 10^{-3}$
$\mu_\alpha(^1D_2)$	$0.2647^c$	$0.2647^d$
$\mu_\alpha(^3D_2)$	$0.2535^c$	$0.2892$
$\mu_\alpha(^3F_2)$	$0.3923^c$	$0.4017$
RMSD ( $\text{cm}^{-1}$ )		$5.7 \times 10^{-3}$

<sup>a</sup>*Ab initio* result from Ref. [56].

<sup>b</sup>The uncertainty represents  $1\sigma$  in the fit and does not include the  $0.015 \text{ cm}^{-1}$  uncertainty in the VUV calibration.

<sup>c</sup>From Ref. [34].

<sup>d</sup>Held at the value of Ref. [34].

analysis of the  $^{83}\text{Kr}$  spectrum was carried out in three steps. First, the positions of the four hyperfine components of the  $\text{Kr}^+$   $^2P_{3/2}$  state, i.e., the ionization energy and the hyperfine constants  $A_{J^+=3/2}$  and  $B_{J^+=3/2}$  [see Eq. (12)] were determined in a nonlinear fit using the positions of the fully resolved hyperfine structure components of the  $ns[3/2]_1$  states. The resulting constants are summarized in Table III and were used to draw the schematic diagram presented in Fig. 1. The hyperfine constants are compared to, and found to be in good agreement with, early and as yet untested *ab initio* calculations of Fraga *et al.* [56]. Second, a forward simulation of the spectrum based on Eqs. (14), (18), and (19) was performed to assign the remaining features, in particular those associated with the  $J=2$  and 3 states. A good agreement between calculated and experimental line positions and intensities could be reached immediately, providing direct evidence for the reliability of our MQDT model and of the  $J=1$  parameter sets derived from the spectrum of  $^{84}\text{Kr}$ . The positions of the  $nd[3/2,5/2]_2$  and  $nd[5/2,7/2]_3$  components, however, appeared systematically shifted, indicating the need for a slight adjustment of the eigen quantum defects of Ref. [34] in the region investigated here. In the last step, we attempted to fit the  $J=2$  and 3 eigen quantum defects to reach a quantitative agreement between MQDT calculation and experiment for these levels also. This last step turned out to be partially successful for the  $J=2$  levels (see Table III), but our spectrum did not contain enough information to derive a statistically meaningful set of eigen quantum defects for the  $J=3$  levels.

Table III summarizes all parameters that could be derived from our least-squares fits of the hyperfine structure of  $^{83}\text{Kr}$ . Not only are the spectral positions very well reproduced by our MQDT calculations but the intensities are also faithfully accounted for, as illustrated in Fig. 3. Moreover, the hyper-

fine coupling constants of the  $^2P_{3/2}$  ground state of  $^{83}\text{Kr}^+$  could be determined.

The following conclusions can be drawn from the MQDT analysis of the Rydberg spectrum of  $^{83}\text{Kr}$ .

(1) Our MQDT treatment of the hyperfine structure based on close-coupling parameters derived from the spectrum of  $^{84}\text{Kr}$  enables a quantitative description of the positions and intensities of the transitions to the  $s$  and  $d$  Rydberg series measured in the single-photon VUV excitation spectrum of  $^{83}\text{Kr}$ .

(2) Whereas the single-photon VUV excitation spectrum of  $^{84}\text{Kr}$  contains information on only the  $J=1$  channels, the spectrum of  $^{83}\text{Kr}$  also contains information on the  $J \neq 1$  channels, and allowed the determination of improved eigenquantum defects for the  $J=2$  channels. Because the close-coupling MQDT parameters are isotope independent in our model, they are valid for all isotopes of Kr.

(3) The origin of the complex hyperfine structure of the Rydberg states lies primarily in the ionic hyperfine interaction, and MQDT provides an adequate framework to determine the ionic hyperfine structure from the analysis of the Rydberg spectrum.

## V. DISCUSSION

The results presented in Sec. IV demonstrate that our MQDT model is well suited to describing the hyperfine structure in the Rydberg spectrum of  $^{83}\text{Kr}$ . The model could be used successfully to determine, by extrapolation, the hyperfine structure of the  $^2P_{3/2}$  ground state of  $\text{Kr}^+$ . Somewhat unexpectedly, the hyperfine structure of the Rydberg states in the range  $n=34\text{--}69$  was found to be equally well reproduced in calculations based on the assumption of purely  $LS$ -coupled eigenchannels as in calculations using the channel mixing parameters  $V_{\bar{\alpha}\alpha}$  derived by Aymar *et al.* [34]. This observation does not imply that the channel mixings are unimportant, but, rather, that the  $V_{\bar{\alpha}\alpha}$  matrix elements are not known accurately enough to reproduce the details of the hyperfine structure in the range of principal quantum number investigated here.

The results for both  $^{84}\text{Kr}$  and  $^{83}\text{Kr}$  suggest (1) that currently known MQDT parameters, while adapted to describing the Rydberg state structure over narrow energy ranges, do not provide a fully satisfactory description over the whole energy range where bound Rydberg states can be probed experimentally, and (2) that the number of MQDT parameters is too large to be determined from available experimental data.

While very encouraging as far as the modeling by MQDT of the hyperfine structure in Rydberg state spectra and the determination of ionic hyperfine structure are concerned, our study led to the determination of only a fraction of all MQDT parameters needed to fully describe the Rydberg spectrum of krypton. It is mainly the energy dependence of the MQDT parameters  $V_{\bar{\alpha}\alpha}$  and  $\mu_{\alpha}$  that appears to be underdetermined.

The questions that are not answered by the results presented so far in this article are (1) whether, and how well, the parameter sets summarized in Table II and III can be used to

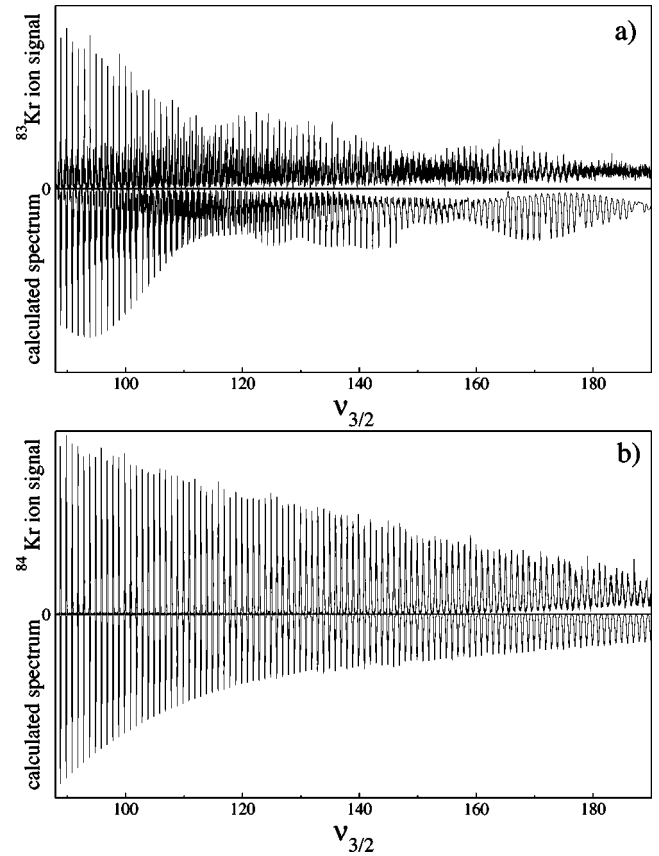


FIG. 4. Comparison of experimental and calculated Rydberg spectra of (a)  $^{83}\text{Kr}$  and (b)  $^{84}\text{Kr}$  in the range of principal quantum number  $n=90\text{--}190$  below the  $^2P_{3/2}$  ground state of  $\text{Kr}^+$  recorded following single-photon excitation from the  $^1S_0$  ground state. The inverted spectra represent MQDT simulations based on MQDT parameters and ionic hyperfine coupling constants determined in a least-squares-fit procedure based on the experimental line positions. A Gaussian line shape with a full width at half maximum of  $0.011\text{ cm}^{-1}$  was assumed in the simulations.

predict the hyperfine structure outside the range  $n=30\text{--}100$  where it has been optimized, (2) whether the interactions between  $LS$ -coupled channels (in particular the  $s$ - $d$  interaction) influences the hyperfine structure, and, if so, how such interactions are likely to manifest themselves in experimental spectra, and (3) whether a complete set of MQDT parameters can be extracted at all from experimental data. These questions are addressed in the next subsections.

### A. The hyperfine structure of $^{83}\text{Kr}$ at $n \geq 100$

Apart from the splitting of the  $ns[3/2]_1$  resonances into three components with  $F=7/2, 9/2,$  and  $11/2$ , the spectrum of  $^{83}\text{Kr}$  in the range  $n \leq 35$  is very similar to that of  $^{84}\text{Kr}$ , and differences become apparent only in measurements at very high resolution. At high  $n$  values, the spectra of the two isotopes differ radically. A comparison of the single-photon spectra of the  $s$  and  $d$  Rydberg series of  $^{83}\text{Kr}$  and  $^{84}\text{Kr}$  in the range  $n=90\text{--}190$  is presented in Fig. 4. Whereas the intensity distribution in the spectrum of the  $^{84}\text{Kr}$  isotope [Fig. 4(b)] follows the pattern typical for Rydberg series at high  $n$ ,

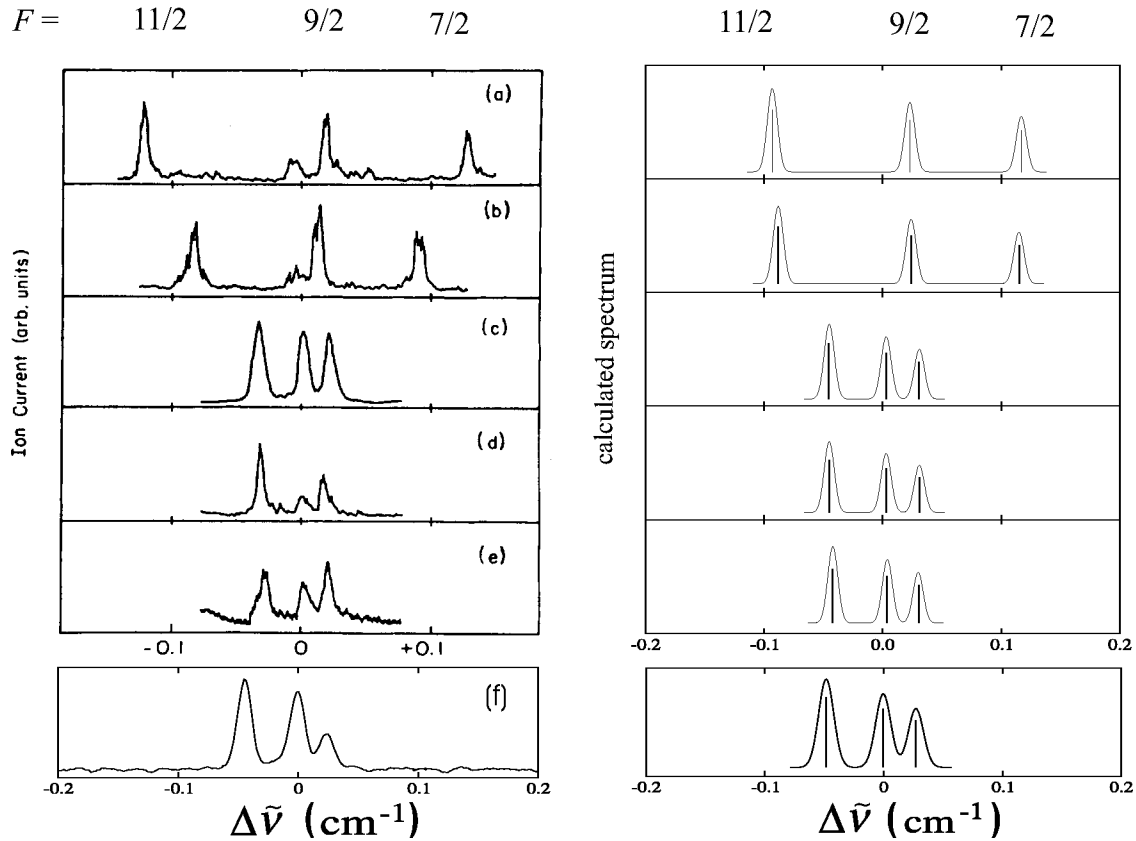


FIG. 5. Comparison of experimental spectra (left-hand side) and MQDT simulations (right-hand side) of the hyperfine structure of  $ns'[1/2]_1$  Rydberg states with (a)  $n=5$ , (b)  $n=6$ , and  $ns[3/2]_1$  Rydberg states with (c)  $n=5$ , (d)  $n=6$ , (e)  $n=7$  and (f)  $n=12$ . The experimental spectra (a)–(e) have been adapted from Ref. [11]. For the comparison, the origin of the horizontal scale has been set, in each spectrum, to the center of gravity of the hyperfine structure.

i.e., a monotonic intensity decrease with increasing  $n$  (the intensities scale as  $1/n^3$ ), until the series can no longer be resolved and the spectrum becomes continuous, the spectrum of  $^{83}\text{Kr}$  [upper spectrum in Fig. 4(a)] reveals a rich structure with intensity fluctuations reminiscent of a beat pattern. A similar behavior was observed in the high-Rydberg-state spectrum of Ba by Beigang *et al.* [10] and can be attributed to the overlap and to local interactions of Rydberg series converging to closely spaced limits. The maxima in the “beat” pattern correspond to regions in which the positions of the members of the Rydberg series converging on different thresholds coincide.

Our MQDT calculations [lower inverted trace in Fig. 4(a)] reproduce the overall intensity patterns satisfactorily with the parameter sets presented in Tables II and III. As explained in our investigation of  $\text{NH}_3$  where a similar behavior was observed in series converging on neighboring spin-rotational states of the  $\text{NH}_3^+$  ion [57], the beat pattern turns out to be very sensitive to the relative positions of the ionic states to which the series converge. The good agreement between our MQDT calculations and the experimental data at high  $n$  values therefore demonstrates the reliability of the hyperfine structure constants determined for the  $^2P_{3/2}$  ground state of  $^{83}\text{Kr}^+$  (see Table III).

The excellent accord between our MQDT calculations and the experimental data at high  $n$  values is not unexpected. The

high- $n$  Rydberg states lie energetically very close to those (with  $n$  in the range 30–100) that have been used to derive the MQDT parameters listed in Tables II and III. Consequently, the fact that the energy dependence of the MQDT parameters is not known precisely has no significant effect on the spectra.

### B. The hyperfine structure of $^{83}\text{Kr}$ at low $n$

Our set of MQDT parameters is less suitable to describe the low- $n$  region of the spectrum because the energy dependence of the MQDT parameters and the departure of the eigenchannels from purely  $LS$ -coupled channels plays a much more important role in this region. The eigen quantum defects and ionic hyperfine structure constants listed in Tables II and III can nevertheless be used to predict the general appearance of the hyperfine structure at low  $n$  values. Such predictions for the  $ns$  series with  $n=5, 6, 7$ , and  $12$  are presented in the bottom four spectra on the right-hand side of Fig. 5 and are compared with the experimental results (shown on the left-hand side of Fig. 5) on the  $5s$ ,  $6s$ , and  $7s$  levels reported by Trickl *et al.* [11] and with a measurement of the  $12s$  level carried out in our laboratory by  $1_{\text{VUV}}+1_{\text{vis}}$  resonance-enhanced two-photon ionization spectroscopy [58]. Because of our inability to account for the energy dependence of the MQDT parameters, the absolute positions of

the Rydberg levels are not predicted well by our calculations, with deviations between calculated and experimental positions being largest for the  $5s$  levels ( $881\text{ cm}^{-1}$ ) and gradually decreasing at higher  $n$  values ( $33.6\text{ cm}^{-1}$  for the  $6s$ ,  $27.1\text{ cm}^{-1}$  for the  $7s$ , and  $1.3\text{ cm}^{-1}$  for the  $12s$  level). The relative positions and intensities of the hyperfine structure components, however, appear to be in almost quantitative agreement, with the exception of the central ( $F=9/2$ ) components in the spectra of the  $n=6$  and  $7$  levels, the intensities of which are overestimated in the calculation. The overall good agreement of the hyperfine splittings, however, demonstrates convincingly that these splittings have their origin in the ionic hyperfine structure, even for the lowest values of the principal quantum number.

Trickl *et al.* [11] have also reported spectra of the hyperfine structure of the  $5s'$  and  $6s'$  Rydberg levels which have been redrawn at the top of Fig. 5 where they are compared with our MQDT predictions. Unfortunately, the experimental hyperfine structures in these spectra could be accounted for only qualitatively by our calculations, which do not satisfactorily reproduce the decrease of the hyperfine structure intervals observed as  $n$  increases from 5 to 6. This deviation is likely to have its origin in a perturbation of either the  $5s'$  or the  $6s'$  level (or both) by neighboring  $ns$  and  $nd$  levels and may provide a handle to extract information on the  $V_{\bar{\alpha}\alpha}$  matrix elements and their energy dependences.

Despite this discrepancy, a rough estimate of the  $A_{J^+=1/2}$  hyperfine coupling constant of the  $^2P_{1/2}$  state of  $\text{Kr}^+$  can be derived using our MQDT model. Adopting the assignment of Trickl *et al.* [11] and depending on whether the  $5s'$  or the  $6s'$  level is assumed to be predominantly perturbed, one obtains values of  $-0.036$  and  $-0.051\text{ cm}^{-1}$  for  $A_{J^+=1/2}$ , respectively. Inclusion of all hyperfine structure intervals observed in traces (a) and (b) of Fig. 5 in the fit yields  $A_{J^+=1/2} = -0.044\text{ cm}^{-1}$ . We suspect that the  $5s'$  level is the more likely level to be perturbed and that the value of  $A_{J^+=1/2}$  lies closer to  $-0.036$  than to  $-0.051\text{ cm}^{-1}$ . The magnetic dipole coupling constant of the  $^2P_{1/2}$  ionic level is thus about five times larger than that of the  $^2P_{3/2}$  level, a behavior that is similar to that observed in the  $^2P$  ground state of the isoelectronic halogen atoms [59,60] (see, for instance, Fig. 4 of Ref. [59]).

### C. The hyperfine structure of $^{83}\text{Kr}$ and the $s$ - $d$ interaction

Thanks to the energy level splittings that arise in  $^{83}\text{Kr}$  from the additional interactions with the nuclear spin, close encounters between  $s$  and  $d$  levels are more likely in  $^{83}\text{Kr}$  than in the  $I=0$  isotopes, particularly at high  $n$  values, giving rise to the possibility of obtaining additional information on the  $s$ - $d$  interaction. The MQDT formalism presented in Sec. III B can be used to investigate theoretically the effect of the  $s$ - $d$  interaction on the appearance of the spectrum of  $^{83}\text{Kr}$ , for example, by setting selected  $V_{\bar{\alpha}\alpha}$  matrix elements to zero in a reference calculation that is then compared with a calculation in which the same elements are held to a non-zero value. This procedure was used to obtain a qualitative picture of the role of the  $s$ - $d$  interaction on the hyperfine structure of the Rydberg states of  $^{83}\text{Kr}$  and is discussed in this subsection.

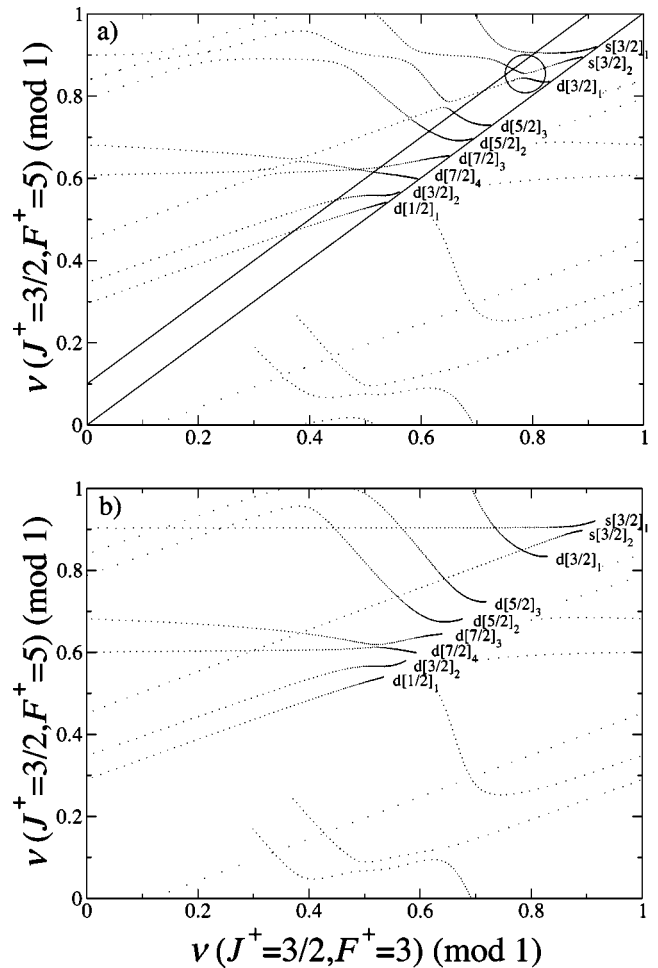


FIG. 6. Theoretical investigation of the role of the  $s$ - $d$  interaction in the hyperfine structure in Rydberg states of  $^{83}\text{Kr}$ . The two panels represent Lu-Fano plots based on calculated energies of the hyperfine structure components of the  $ns$  and  $nd$  Rydberg states with  $F=11/2$  located below the  $^2P_{3/2}$  ground state of  $\text{Kr}^+$ . The energies were calculated (a) using the  $V_{\bar{\alpha}\alpha}$  matrix elements determined by Aymar *et al.* [34] and (b) assuming that the eigenchannels are exactly  $LS$  coupled, i.e., neglecting channel mixings. The encircled area in (a) indicates a region where the  $s$ - $d$  interaction may be characterized experimentally. The two diagonal lines in (a) indicate the range of  $n$  values between 30 and 80 where resolved information on the hyperfine structure could be determined in the present experiments. The blank area below the diagonal of the plot originates from the fact that only states with  $n \leq 130$  were used.

The results of our MQDT calculations on the role of the  $s$ - $d$  interaction turned out to be particularly easy to compare when represented in the form of the Lu-Fano plots [61] displayed in Fig. 6. To generate the Lu-Fano plots of Fig. 6, the position of each calculated energy level was used to first derive the fractional part of two effective quantum numbers  $\nu_{J^+F^+}$  defined relative to distinct ionic hyperfine levels using Eq. (14), and, second, to set a point in a two-dimensional plot with coordinates corresponding to the fractional part of these effective quantum numbers. Rydberg series in Lu-Fano plots appear as sets of points forming trajectories, and the interactions between the series manifest themselves as avoided crossings between these trajectories, several of

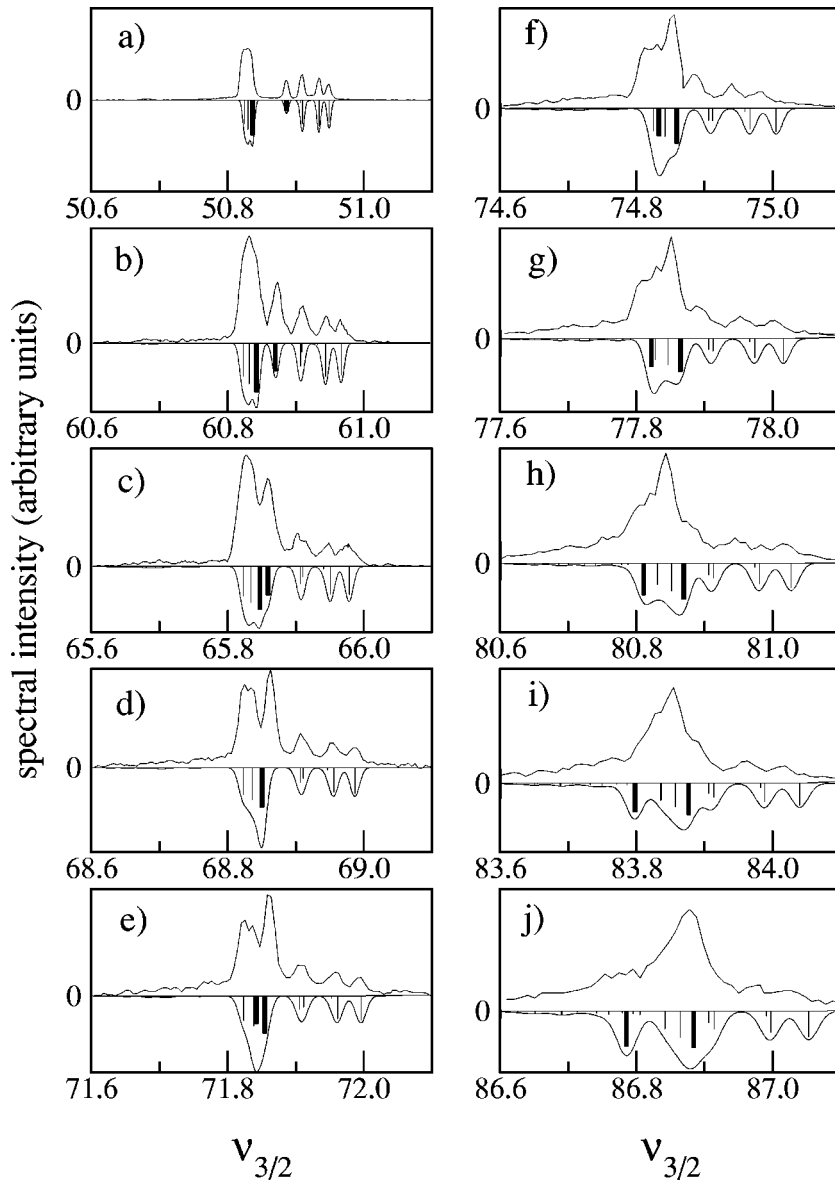


FIG. 7. The hyperfine structure in the region of the (anti)crossing between the  $(n+2)s[3/2] \times (J=2, F=11/2)$  and the  $nd[3/2](J=1, F=11/2)$  levels corresponding to the encircled area in Fig. 6(a). The inverted traces represent MQDT simulations which assume that the eigenchannels are purely  $LS$  coupled. For comparison, the spectra are displayed as a function of the effective principal quantum number  $\nu_{3/2}$  defined with respect to the center of gravity of the hyperfine structure of the  $^2P_{3/2}$  ground state of  $^{83}\text{Kr}^+$ . The effect of the  $s$ - $d$  interaction can be recognized from the fact that the experimental spectrum shows an intensity minimum in (d) at the position where the calculated positions of the  $(n+2)s[3/2](J=2, F=11/2)$  and  $nd[3/2](J=1, F=11/2)$  levels become degenerate.

which are immediately recognized by inspecting Fig. 6.

The Lu-Fano plots displayed in Fig. 6 were obtained by deriving the effective quantum numbers of the  $F=11/2$  levels with respect to the  $F^+=3$  and  $F^+=5$  hyperfine structure levels of the  $^2P_{3/2}$  ground state of  $^{83}\text{Kr}$ . Similar plots, with the same information content, can also be drawn by defining the effective quantum numbers with respect to the  $F^+=4$  and 6 levels.

In the first model calculation, leading to the results presented in Fig. 6(b), the  $V_{\bar{\alpha}_F \alpha_F}$  matrix was set to unity (i.e., the close-coupling eigenchannels were assumed to be exactly  $LS$  coupled). The trajectories representing the various Rydberg series can thus be labeled by the values of  $\ell$  (either  $s$  or  $d$ ) and  $J$ . The trajectories have their origin along the diagonal of the plot which corresponds to the low- $n$  limit. As expected, the trajectories corresponding to  $s$  and  $d$  series all cross exactly in Fig. 6(b). The area between the two diagonal lines represents the range of  $n$  values for which resolved data could be obtained in the present experiments. The blank area

below the diagonal of the Lu-Fano plot stems from the fact that, for clarity, the states beyond  $n=130$  were not used.

In the second model calculation [Fig. 6(a)], the  $V_{\bar{\alpha}_F \alpha_F}$  matrix was taken from the work of Aymar *et al.* [34]. Although the overall appearance of the Lu-Fano plot resembles that shown in Fig. 6(b), several avoided crossings are clearly observable, corresponding to interactions between channels differing either in the value of  $J$  only or in the value of both  $\ell$  and  $J$  [see encircled region in Fig. 6(a)], the latter being a manifestation of the  $s$ - $d$  interaction. It is important to realize that, whereas in the  $I=0$  isotopes, the  $s$ - $d$  interaction manifests itself only by level shifts and intensity perturbations affecting levels of the same  $J$  value, in  $^{83}\text{Kr}$  the  $s$ - $d$  interaction also causes perturbations between levels of different  $J$  values and is therefore much easier to detect.

The Lu-Fano plots displayed in Fig. 6 provide a convenient way to analyze the channel interactions in krypton and to identify spectral regions where specific interactions ought to be observable in high-resolution spectra. A set of spectra

of  $^{83}\text{Kr}$  in the region corresponding to the encircled area of Fig. 6(a) is displayed in Fig. 7. In this region, the  $s$  ( $J=2, F=11/2$ ) channel interacts with the  $d$  ( $J=1, F=11/2$ ) channel. The interaction, which manifests itself by the avoided crossing in Fig. 6(a), is also clearly visible in the experimental spectra. To facilitate the comparison of spectra recorded at different values of  $n$ , the spectral intensities were plotted as a function of the effective principal quantum number defined with respect to the center of gravity of the hyperfine structure of the  $^2P_{3/2}$  ground state of  $^{83}\text{Kr}$ . The experimental spectra are compared, in each panel of Fig. 7, with inverted calculated stick spectra and the corresponding intensity envelopes. Unfortunately, the values of the  $V_{\bar{\alpha}\alpha}$  matrix elements reported by Aymar *et al.* [34] were not accurate enough to reproduce the experimental positions and intensities satisfactorily, and it turned out to be more convenient, to recognize the effects of the  $s$ - $d$  interaction, to compare the experimental spectra with calculations based on the assumption of a unit  $V_{\bar{\alpha}\alpha}$  matrix and on the parameter sets derived from our high-resolution measurements (see Tables II and III). The positions and intensities of the members of the two interacting  $[(n+2)s$  ( $J=2, F=11/2$ ) and  $nd$  ( $J=1, F=11/2$ )] series are represented by the bold vertical lines in Fig. 7. At  $n$  values around 50, the spectra reveal a broad feature associated with the three (unresolved) components of  $nd[3/2]_1$ , three well-resolved lines corresponding, in order of ascending effective principal quantum number, to the  $(n+2)s[3/2]_1, F=11/2, 9/2$ , and  $7/2$  hyperfine structure components, and the weaker  $(n+2)s(J=2, F=11/2)$  component already discussed in Sec. IV B. As  $n$  increases from 50 to 90, the position of the  $(n+2)s(J=2, F=11/2)$  moves across the  $nd[3/2]_1$  manifold to reappear on the low-energy side beyond  $n=80$ . At this point, channel mixings induced by the hyperfine interactions lead to a large number of hyperfine structure components to become optically accessible.

The effect of the  $s$ - $d$  interaction is most clearly recognized at the position, around  $\nu_{3/2} \approx 69$  [see panel (d) in Fig. 7], where the calculated positions of the  $(n+2)s(J=2, F=11/2)$  and  $nd(J=1, F=11/2)$  series almost exactly coincide. In the experimental spectrum, however, an intensity minimum separating two strong lines is observed at this position and indicates the avoided crossing between the two interacting series.

Although the comparison of experimental and calculated spectra displayed in Fig. 7 enables the direct observation of the effect of the  $s$ - $d$  interaction, the experimental data turned out not to be sufficient to extract unambiguous and statistically well-defined values for the relevant  $V_{\bar{\alpha}\alpha}$  matrix elements. A very high-resolution study of this spectral region by millimeter-wave spectroscopy, following the same strategy as used to study the hyperfine structure in the Rydberg spectrum of  $\text{H}_2$  [16–18], is currently under way to obtain more detailed information on this very interesting and complex part of the Rydberg spectrum of  $^{83}\text{Kr}$ .

## VI. CONCLUSIONS

Multichannel quantum defect theory represents a powerful tool to analyze the hyperfine structure in Rydberg states.

Because the effects of the hyperfine interactions are negligible in the close-coupling region of the electron-core collision, the close-coupling MQDT parameters necessary to predict the hyperfine structure of Rydberg states are identical to those needed to calculate the Rydberg level structure in isotopes (or isotopomers, in the case of molecules) with zero nuclear spin.

The theory enables the parametrization of the hyperfine structure in terms of the hyperfine coupling constants of the ion core. If these constants are known, MQDT can be used to predict the hyperfine structure at any value of the principal quantum number  $n$ . If the hyperfine coupling constants are not known, they can be determined from the measured hyperfine structure of Rydberg states. Direct measurements of the hyperfine structure of molecular ions by high-resolution spectroscopy are notoriously difficult, primarily because of problems associated with space-charge effects which limit the ion density in the experiment volume and can cause undesirable Doppler broadenings. Measurements of the hyperfine structure in Rydberg states of the neutral parent species are not subject to these limitations. When combined with MQDT, such measurements provide an attractive alternative to determine the ionic hyperfine structure. In the case of  $^{83}\text{Kr}^+$  discussed in this article, high-resolution spectroscopy and MQDT of the Rydberg level structure has enabled a determination of the hyperfine structure in the  $^2P$  ground electronic state.

Thanks to the relaxation of the selection rules on  $\Delta J$  and the additional splittings in the energy level structure caused by the hyperfine interactions, high-resolution spectroscopy of the hyperfine structure in Rydberg states facilitates the observation of channel interactions, such as the  $s$ - $d$  interaction in krypton, that can be difficult to observe in isotopes (or isotopomers) with  $I=0$ .

Whereas MQDT appears very well suited to describe the energy level structure of Rydberg states, little is known so far about the role of the hyperfine structure in the dynamics of atomic and molecular Rydberg states, although first results indicate that neighboring hyperfine structure components can be subject to different decay processes and have very different lifetimes [14]. The formalism used in this article represents a step toward a better understanding and a formal treatment of the role of the nuclear spins in the decay dynamics of Rydberg states, and may turn out to be important for other lines of scientific investigation such as studies aiming at understanding the properties of cold Rydberg gases [62–64] and at controlling the translational motion of Rydberg atoms and molecules in inhomogeneous electric fields [35,65].

## ACKNOWLEDGMENTS

We thank Dr. G. M. Greetham, Dr. A. Osterwalder, and A. Wüest (ETH Zürich) for useful discussions and Dr. Ch. Jungen (Orsay) for valuable exchanges on the treatment, by MQDT, of the hyperfine structure in Rydberg states. This work was supported financially by the Swiss National Science Foundation and the ETH Zürich.

- [1] M. J. Seaton, Rep. Prog. Phys. **46**, 167 (1983).
- [2] U. Fano and A. R. P. Rau, *Atomic Collisions and Spectra* (Academic, Orlando, FL, 1986).
- [3] M. Aymar, C. H. Greene, and E. Luc-Koenig, Rev. Mod. Phys. **68**, 1015 (1996).
- [4] *Molecular Applications of Quantum Defect Theory*, edited by Ch. Jungen (Institute of Physics Publishing, Bristol, 1996).
- [5] Ch. Jungen and G. Raseev, Phys. Rev. A **57**, 2407 (1998).
- [6] K. T. Lu, Phys. Rev. A **4**, 579 (1971).
- [7] J.-Q. Sun, Phys. Rev. A **40**, 7355 (1989).
- [8] J.-Q. Sun and K. T. Lu, J. Phys. B **21**, 1957 (1988).
- [9] J.-Q. Sun, K. T. Lu, and R. Beigang, J. Phys. B **22**, 2887 (1989).
- [10] R. Beigang, W. Makat, A. Timmermann, and P. J. West, Phys. Rev. Lett. **51**, 771 (1983).
- [11] T. Trickl, M. J. J. Vrakking, E. Cromwell, Y. T. Lee, and A. H. Kung, Phys. Rev. A **39**, 2948 (1989).
- [12] D. Uy, C. M. Gabrys, T. Oka, B. J. Cotterell, R. J. Stickland, Ch. Jungen, and A. Wüest, J. Chem. Phys. **113**, 10 143 (2000).
- [13] F. Brandi, W. Hogervorst, and W. Ubachs, J. Phys. B **35**, 1071 (2002).
- [14] F. Merkt and A. Osterwalder, Int. Rev. Phys. Chem. **21**, 385 (2002).
- [15] F. Merkt, R. Signorell, H. Palm, A. Osterwalder, and M. Somavilla, Mol. Phys. **95**, 1045 (1998).
- [16] A. Osterwalder, R. Seiler, and F. Merkt, J. Chem. Phys. **113**, 7939 (2000).
- [17] A. Osterwalder, Dissertation No. 14551, ETH, Zürich, 2002.
- [18] A. Osterwalder, A. Wüest, F. Merkt, and Ch. Jungen (unpublished).
- [19] C. E. Moore, *Atomic Energy Levels*, Natl. Bur. Stand. (U.S.) Circ. No. 467 (U.S. GPO, Washington, D.C., 1952), Vol. II, p. 170.
- [20] V. Kaufman and C. J. Humphreys, J. Opt. Soc. Am. **59**, 1614 (1969).
- [21] J. Sugar and A. Musgrove, J. Phys. Chem. Ref. Data **20**, 859 (1991).
- [22] H. Beutler, Z. Phys. **93**, 177 (1935).
- [23] K. Radler and J. Berkowitz, J. Chem. Phys. **70**, 216 (1979).
- [24] K. Yoshino and Y. Tanaka, J. Opt. Soc. Am. **69**, 159 (1979).
- [25] U. Hollenstein, R. Seiler, and F. Merkt, J. Phys. B **36**, 893 (2003).
- [26] C. Delsart, J.-C. Keller, and C. Thomas, J. Phys. B **14**, 4241 (1981).
- [27] D. Klar, K. Harth, J. Ganz, T. Kraft, M.-W. Ruf, H. Hotop, V. Tsemekhman, K. Tsemekhman, and M. Ya Amusia, Z. Phys. D: At., Mol. Clusters **23**, 101 (1992).
- [28] S. Yoon and W. L. Glab, J. Phys. B **27**, 4133 (1994).
- [29] M. Ahmed, M. A. Zia, M. A. Baig, and B. Suleman, J. Phys. B **30**, 2155 (1997).
- [30] R. Kau, I. D. Petrov, V. L. Sukhorukov, and H. Hotop, J. Phys. B **31**, 1011 (1998).
- [31] D. Klar, M. Aslam, M. A. Baig, K. Ueda, M.-W. Ruf, and H. Hotop, J. Phys. B **34**, 1549 (2001).
- [32] J. Geiger, Z. Phys. A **282**, 129 (1977).
- [33] M. Bounakhla, J. P. Lemoigne, J. P. Grandin, X. Husson, H. Kucal, and M. Aymar, J. Phys. B **26**, 345 (1993).
- [34] M. Aymar, O. Robaux, and C. Thomas, J. Phys. B **14**, 4255 (1981).
- [35] D. Townsend, A. L. Goodgame, S. R. Procter, S. R. Mackenzie, and T. P. Softley, J. Phys. B **34**, 439 (2001).
- [36] C.-M. Lee and K. T. Lu, Phys. Rev. A **8**, 1241 (1973).
- [37] W. R. Johnson, K. T. Cheng, K.-N. Huang, and M. Le Dourneuf, Phys. Rev. A **22**, 989 (1980).
- [38] H. H. Fielding and T. P. Softley, J. Phys. B **25**, 4125 (1992).
- [39] R. D. Knight, Phys. Rev. A **34**, 3809 (1986).
- [40] J. Ganz, A. Siegel, W. Bussert, H. Harth, M.-W. Ruf, H. Hotop, J. Geiger, and M. Fink, J. Phys. B **16**, L569 (1983).
- [41] K. Harth, J. Ganz, M. Raab, K. T. Lu, J. Geiger, and H. Hotop, J. Phys. B **18**, L825 (1985).
- [42] H. Kopfermann and N. Wieth-Knudsen, Z. Phys. **85**, 353 (1933).
- [43] H. Korsching, Z. Phys. **109**, 349 (1938).
- [44] W. L. Faust and L. Y. Chow Chiu, Phys. Rev. **129**, 1214 (1963).
- [45] D. A. Jackson, J. Opt. Soc. Am. **67**, 1638 (1977).
- [46] H. Gerhardt, F. Jeschonnek, W. Makat, E. Matthias, H. Rinneberg, F. Schneider, A. Timmermann, R. Wenz, and P. J. West, Hyperfine Interact. **9**, 175 (1981).
- [47] B. D. Cannon and G. R. Janik, Phys. Rev. A **42**, 397 (1990).
- [48] M. Keim, E. Arnold, W. Borchers, U. Georg, A. Klein, R. Neugart, L. Vermeeren, R. E. Silverans, and P. Lievens, Nucl. Phys. A **586**, 219 (1995).
- [49] A. Osterwalder and F. Merkt, Phys. Rev. Lett. **82**, 1831 (1999).
- [50] U. Hollenstein, H. Palm, and F. Merkt, Rev. Sci. Instrum. **71**, 4023 (2000).
- [51] H. Kopfermann, *Nuclear Moments* (Academic, New York, 1958).
- [52] R. N. Zare, *Angular Momentum: Understanding Spatial Aspects in Chemistry and Physics* (Wiley, New York, 1988).
- [53] E. U. Condon and G. H. Shortley, *The Theory of Atomic Spectra* (Cambridge University Press, London, 1953).
- [54] See EPAPS Document No. E-PLRAAN-68-021309 for a table of the positions of the *ns* and *nd* Rydberg states ( $J=1$ ) of  $^{84}\text{Kr}$  and the deviations between observed and calculated levels. A direct link to this document may be found in the article's HTML reference section. This document may also be reached via EPAPS homepage (<http://www.aip.org/pubservs/epaps.html>) or from [ftp.aip.org](ftp://ftp.aip.org) in the directory /epaps/. See the EPAPS homepage for more information.
- [55] See EPAPS Document No. E-PLRAAN-68-021309 for a table of the positions of the *ns* Rydberg states of  $^{83}\text{Kr}$  and the deviations between observed and calculated levels. A direct link to this document may be found in the article's HTML reference section. This document may also be reached via EPAPS homepage (<http://www.aip.org/pubservs/epaps.html>) or from [ftp.aip.org](ftp://ftp.aip.org) in the directory /epaps/. See the EPAPS homepage for more information.
- [56] S. Fraga, K. M. S. Saxena, and B. W. N. Lo, At. Data **3**, 323 (1971).
- [57] R. Seiler, U. Hollenstein, T. P. Softley, and F. Merkt, J. Chem. Phys. **118**, 10024 (2003).
- [58] M. Somavilla, U. Hollenstein and F. Merkt (unpublished).
- [59] Y. He, M. Quack, R. Ranz, and G. Seyfang, Chem. Phys. Lett. **215**, 228 (1993).
- [60] E. Luc-Koenig, C. Morillon, and J. Vergès, Physica (Amsterdam) **70**, 175 (1973).
- [61] K. T. Lu and U. Fano, Phys. Rev. A **2**, 81 (1970).

- [62] I. Mourachko, D. Comparat, F. de Tomasi, A. Fioretti, P. Nosbaum, V. M. Akulin, and P. Pillet, *Phys. Rev. Lett.* **80**, 253 (1998).
- [63] W. R. Anderson, M. P. Robinson, J. D. D. Martin, and T. F. Gallagher, *Phys. Rev. A* **65**, 063404 (2002).
- [64] S. K. Dutta, D. Feldbaum, A. Walz-Flannigan, J. R. Guest, and G. Raithel, *Phys. Rev. Lett.* **86**, 3993 (2001).
- [65] S. R. Procter, Y. Yamakita, F. Merkt, and T. P. Softley, *Chem. Phys. Lett.* **374**, 2528 (2003).